Journal of the European Ceramic Society 43 (2023) 1117–1126

Contents lists available at ScienceDirect

Journal of the European Ceramic Society

journal homepage: www.elsevier.com/locate/jeurceramsoc

Fabrication of powder components with internal channels by spark plasma sintering and additive manufacturing

Elisa Torresani [a,*], Maricruz Carrillo [a,b], Chris Haines [c], Darold Martin [d], Eugene Olevsky [a,b]

[a] San Diego State University, 5500 Campanile Dr., San Diego, CA 92182–1323, USA
[b] University of California San Diego, 9500 Gilman Dr, La Jolla, CA 92093, USA
[c] US Army DEVCOM - Army Research Laboratory, Aberdeen Proving Ground, MD, USA
[d] US Army DEVCOM – Armaments Center, Picatinny Arsenal, NJ, USA

ARTICLE INFO

Keywords:
Spark plasma sintering
Additive manufacturing
Solvent jetting
Cooling channels

ABSTRACT

A novel method of producing complex ceramic and metallic parts with designed internal channels is developed. The method utilizes a combination of the additive manufacturing technique of solvent jetting and spark plasma sintering (SPS.) The developed manufacturing approach brings benefits in producing complex shapes with internal channels. Along with geometric customization of the 3D printed mold, a major advantage of this method is the removal of the need for a long debinding process, usually necessary with other 3D printing methods, by using the SPS. High density ceramic and metallic complex parts with internal channels were successfully produced with close to theoretical densities. The conducted studies include the development of a model that can predict the evolution and/or distortions of the complex-shaped powder assembly during the sintering process. The model is based on the continuum theory of sintering formulations embedded in a finite element code.

1. Introduction

Spark Plasma Sintering (SPS) is a materials processing technology which involves the simultaneous application of pressure and electrical field to consolidate powder materials [1–3]. It is well known for its capability to rapidly densify even traditionally hard-to-sinter materials (such as carbides and other high temperature systems) which cannot be consolidated to high density by conventional sintering technologies. Due to the fast-heating rates that can be reached, it is able to minimize grain growth even when sintering nanoscale powders [4–7]. Despite the SPS technology's potential to produce components with high mechanical properties and tailored microstructures, it is limited to the production of components with simple shapes, such as cylinders. This limitation primarily derives from the inhomogeneity that is usually introduced by the application of pressure to components with complex shapes that have different thickness in the direction of pressing [8–10]. In uniaxial compaction, the thinner areas densify earlier and prevent the punches from completely densifying the entire component [11]. In addition, nonuniformity of temperature and electric current density can also contribute to structure heterogeneities in complex-shape components manufactured by SPS. Different approaches to overcome this limitation have been utilized [8,9,12,13]. Using graphite foil to create an interface between powders during SPS, Manière et al. successfully produced multiple complex shapes simultaneously. This group also developed an imprint method to produce complex net shapes by creating an inert interface between two powders or porous bodies. Lastly, a sacrificial part approach was developed that consists of compacting two powder parts resulting in the desired component and a sacrificial component [9, 13,14]. These methods have extended the range of what can be produced via SPS. However, the focus has been on the net-shaping of the external geometry of the components or very simple internal architectures. But in many applications the fabricated components need to have internal features such as channels or holes.

For applications in the energy sector, there is great interest in manufacturing ultra-high-temperature resistant components, such as turbine blades, to enhance the efficiency of power generation [15–17]. However, the production of components using ultra-high-temperature resistant materials is very costly and difficult via both traditional and additive manufacturing technologies. Therefore, these components integrate design features, such as cooling channels and holes, to increase their efficiency and enable them to be manufactured from less expensive alloys with lower working temperatures. [18–20]. These features are typically produced through laser machining in traditionally manufactured components or are a part of the original design in the components

* Corresponding author.
E-mail address: etorresani@sdsu.edu (E. Torresani).

https://doi.org/10.1016/j.jeurceramsoc.2022.11.008
Received 18 August 2022; Received in revised form 31 October 2022; Accepted 2 November 2022
Available online 4 November 2022

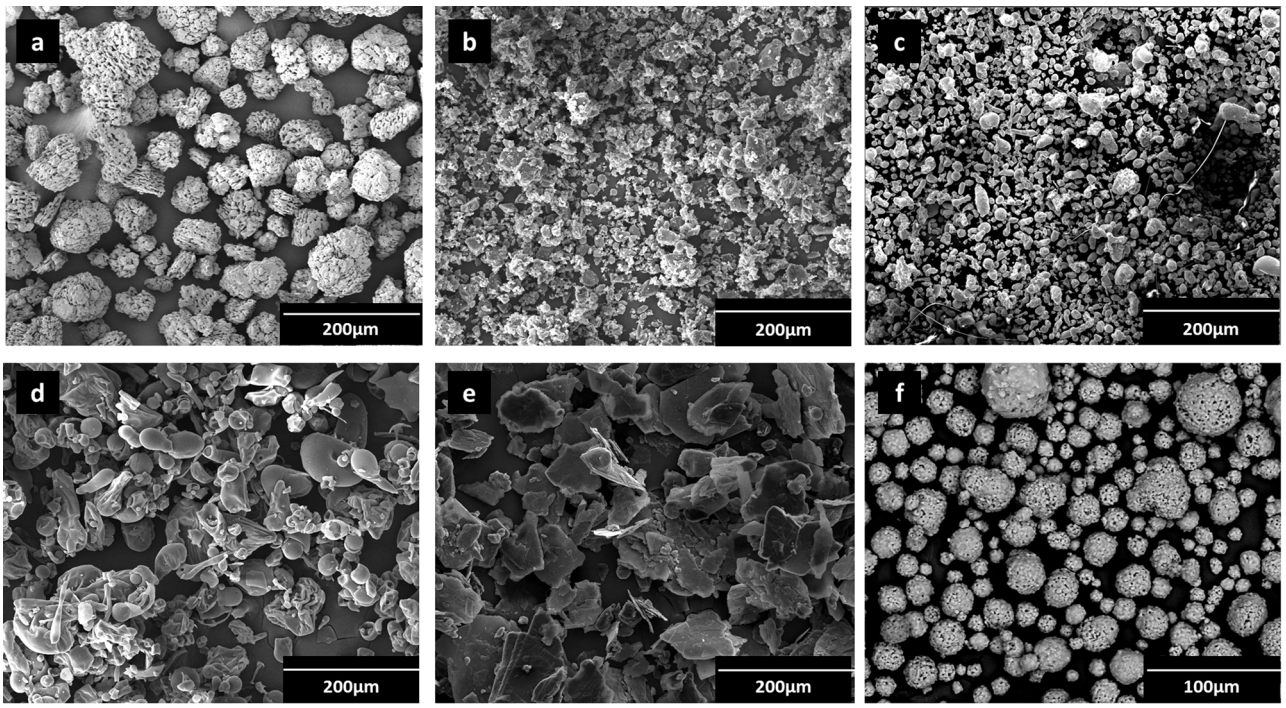

Fig. 1. SEM image of raw powders: a) Alumina, b) Sugar, c) Stainless Steel 316 L, d) Maltodextrin, e) Graphite, f) Hydroxyapatite.

produced through additive manufacturing (AM). Both processes have a few disadvantages. Laser machining is costly and difficult to operate for fragile/brittle materials. Similarly, AM (e.g. SLM/SLS), while allowing the production of components with complex shapes, is time consuming and also requires a post-processing step to remove the thermal stresses and/or refine the microstructure.

Internal channels are also important for ceramic components involved in various energy applications such as solar cells, wind rotors, heat transfer devices, and regenerative cooling system for hypersonic vehicles [21–24]. When considering manufacturing of channels, the main concern is removing material from inside the designed openings. Traditionally in energy applications, ceramic components with channels are made by slip casting or injection molding in two pieces and then joined which inevitably creates locations for potential early failures. Through-hole channels can also be machined into the parts but further add to the cost and processing steps. Self-supported 3D printing techniques, such as binder jetting and stereolithography (SLA), are being considered for parts that require internal channels. Singh et al., chose binder jetting to successfully produce a prototype of a one-piece concentrating solar power ceramic heat exchanger [25], highlighting the advantage of AM by producing a complex internal structure in one print. However, high density was not achieved despite the long debinding and sintering cycles used.

In the biomedical industry, ceramics requiring internal cavities are being used mostly for orthopedic applications such as bone tissue engineering, bone implants and scaffolds. Traditional methods for producing porous implants include salt leaching [26], freeze drying [27], gel or chemical forming [28]. These techniques have limitations in the ability to include or tailor external and internal geometries. Internal architecture is important in mimicking bone because these channels allow nutrient absorption and cell adhesion [29]. AM becomes particularly attractive for orthopedics due to the ability to tailor the geometry of scaffolds and implants to the patient specific injury; however, internal structures and channels are difficult to produce with AM [30]. High density ceramic components with complex external geometries can be designed and produced using printed molds and applying pressure before free sintering as done in previous work [31]. Producing a high-density bio-ceramic however, adds a level of difficulty due to their high melting temperatures, yet low phase transition temperatures. To retain the biocompatibility of Hydroxyapatite (HAP) for example, one must sinter at temperatures below 1300 °C [32].

Microsystems, to include micro-electrical mechanical systems (MEMS) and micro-fluidic devices have been investigated widely in recent years with the demand for smaller components for electronics and testing [33]. Current silicone-based manufacturing methods limit the 3D geometry of the microsystems and have become difficult to source [34]. To address the manufacturing of ceramic microsystems with small internal channels, Do et al., propose using a 0.9 mm thick machined graphite shape, inserting it into alumina powder, pressing them together and then removing the graphite by annealing in air. A micro burner was successfully produced using this approach; however, the geometry of the internal structure was limited by the machining technique used and by the thickness of the graphite sheet. In another study, Nawrot et al., assessed the applicability of Stereolithography to microfluidic devices [35]. Although they were able to successfully create channels with an optimized sintering cycle that limited deformation, the use of SLA required a long debinding time and not all channels were able to fully penetrate the whole structure making this technique non-transferable into high output production situations.

Overall, in traditional ceramic manufacturing, conventional sintering is the most common method for producing ceramics. In additive manufacturing, Stereolithography has been the most common 3D printing method explored for ceramic components with internal channels and cavities [36]. However, there are issues with both traditional and additive manufacturing methods that include the inability to completely remove the polymer binder and long debinding times which, limit the applicability of advanced ceramics in industry. There is opportunity to use advanced sintering methods as a tool to address the shortcomings mentioned above.

In this study, a novel method of producing complex ceramic and metallic parts with designed internal channels is proposed. Using solvent jetting, a graphite structure can be printed to serve as a mold, or shaper, for the powder to be sintered (see Section 2). The powder of interest is then placed inside the mold in the raw form, with no binder or

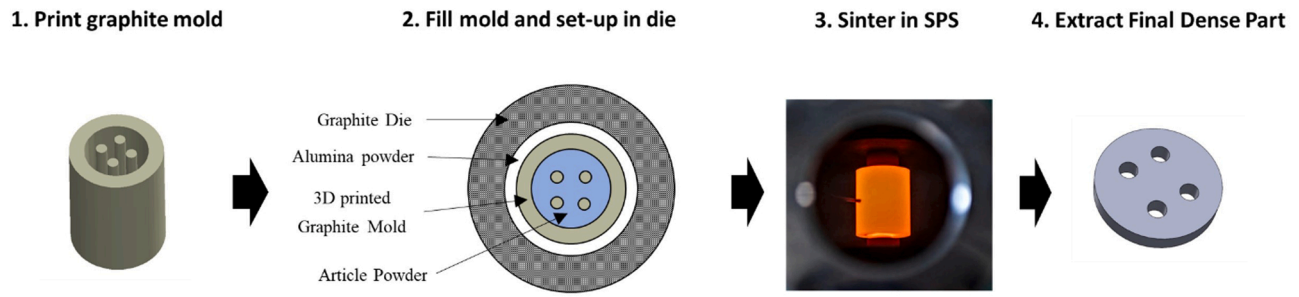

Fig. 2. General experimental procedure.

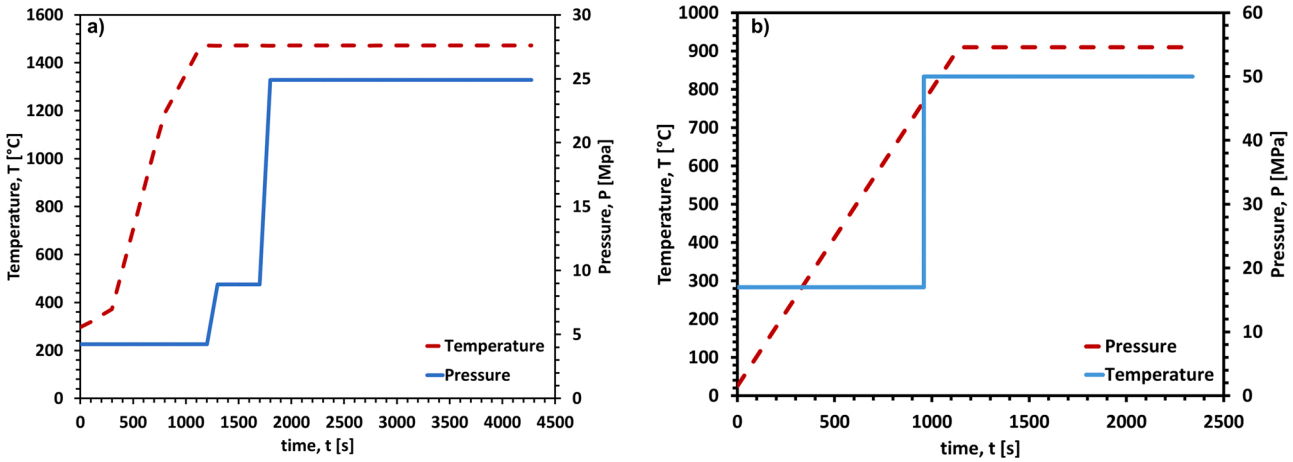

Fig. 3. process parameters used for the SPS process of a) the 4-channels HAP component, b) the Stainless-steel component.

preparation necessary before it is placed in the Spark Plasma Sintering (SPS) machine. This method brings many benefits, particularly for ceramics, in producing complex shapes with internal channels. Along with geometric customization of the 3D printed mold, a major advantage of this method is the removal of the need for a long debinding process that is often necessary with other 3D printing methods. Furthermore, because the graphite does not sinter, it is easily removed from the internal channels and cavities via sand blasting. Any remaining graphite can be decomposed in air via annealing. Additionally, sintering time is drastically reduced using SPS which leads to high density with limited grain growth. Using this novel approach, we successfully sintered to near theoretical density complex ceramic and metallic parts with internal channels (see Sections 2 and 4.). At the same time, the proposed novel approach requires the development of a model that can predict the evolution and/or distortions of the complex-shaped powder assembly during the sintering process (see Section 3.).

SPS is a process where three main physical phenomena are involved and interconnected: densification, thermal distribution and electrical behavior of the specimens. Powder densification can be modeled based on studies presented in literature [11,37–40]. SPS involves Joule heating [41–57], densification and field phenomena [1,11,37,39,58–60]. To simulate the thermal and electrical current distribution and the densification during SPS, Finite Element Method (FEM) is largely used [9,61–64]. The behavior of the powder assembly during the SPS process is predicted using a model based on the continuum theory of sintering [37], which has been embedded in a FEM (finite element model) software and validated through the comparison with the experimental results [1] (see Sections 4 and 5.).

2. Materials and method

The printing powder for the graphite sacrificial mold was prepared in advance by mixing graphite powder (Atlantic Equipment Engineers, 325 mesh) with sugar and maltodextrin in a conventional dry mixer (Turbula®, WAB-Group, Switzerland) for 60 min. The main component of the powder was graphite making up 75 wt% of the mixture; powdered sugar (Wholesome) and maltodextrin (Pure Organic) were used as binders with the combined make up of 25 wt% of the mixture (12.5% sugar and 12.5% maltodextrin). Alumina powder (Materion, Al2O3 99.2% pure, 325 mesh, Phoenix, AZ, USA) was used as an electrical insulator to stabilize the temperature within the mold and therefore protect the ceramic powder of interest from thermal shock. Hydroxyapatite (HAP, CAPTAL 30, Plasma Biotal Limited, United Kingdom) and Stainless Steel (SS316L, OzoMetal, USA) were chosen as the powders to be sintered for this study. The morphology and particle size of each powder are shown in Fig. 1.

A general overview of the experimental procedure is shown in Fig. 2. First, the graphite mold was printed in a custom-made solvent jetting printer using the mixed graphite-sugar-maltodextrin powder. Printer resolution greatly depends on the size and morphology of the powders; in the current work, the resolution of the mold is relatively low due to the “flake-like” shape of the graphite powder. In some applications, the roughness of the surface is desirable,- for example in the orthopedic implant industry. In the case where no roughness is desired, a post processing step might be necessary. The water-based ink which is contained in HP 45 Inkjet cartridges was composed of 8.3 vol% of Isopropyl alcohol, 8.3 vol% of diethylene-glycol and 83.4 vol% of DI water. First, the powder layer was spread, then the inkjet cartridge sprayed water-based ink in the designated areas for that layer (dictated by the CAD model) activating the binder and “gluing” the ceramic particles together. This process was repeated layer by layer until the printed object was completed. Note: printing times range from 30 min to 3 h depending on the geometry of the scaffold and, more importantly, on the height and layer height setting used. Finally, the printed samples were

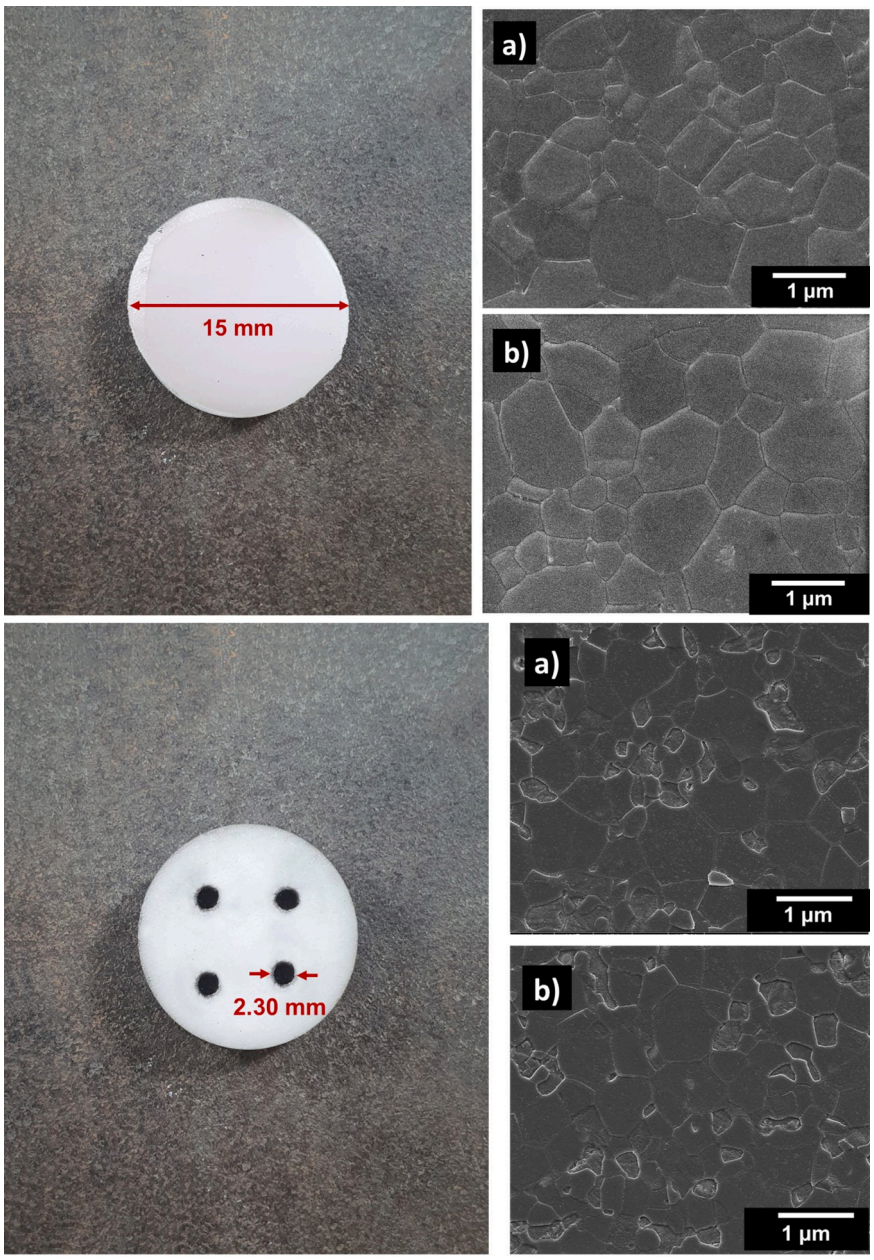

Fig. 4. Final HAP cylindrical sample with four channels and with no channels showing SEM of the homogeneous and heterogenous microstructure, respectively. The small grain sizes can also be observed in both samples a) center and b) edge.

cured in a furnace at 80 °C for 30 min to ensure the samples were dried before using pressurized air to remove loose powder.

Prior to sintering, the mold was subjected to partial debinding in vacuum for one hour at 850 °C. The mold was then filled with a powder of interest and processed via Spark Plasma Sintering. The SPS device used was the SPSS DR.SINTER Fuji Electronics model 515, Japan. After sintering, the graphite mold was easily scraped off due to its higher sintering temperature compared to the subject powders (Fig. 2). The part was initially cleaned using compressed air and tweezers (for internal channels) and then surface polished if necessary. The sample set-up and cleaning process for metallic and ceramic powders differed slightly and will be described separately below.

Hydroxyapatite (HAP) was chosen as a proof of concept for using this method with ceramic materials due to its biocompatibility and potential use in biomedical applications. HAP is a delicate material that must remain under 1300 °C to avoid a phase transformation which diminishes its biocompatibility, therefore, extra precaution was taken using the SPS device by electrically insulating it with alumina powder. A 35 mm diameter graphite die was used for the tooling to surround the graphite mold containing HAP powder with alumina powder. A small piece of graphite paper is placed on top of the graphite mold to keep alumina powder from entering the graphite mold where the HAP powder is located. Alternatively, a graphite lid could also be printed to use in place of the graphite paper if a more complex shape is desired. For other materials, the alumina powder might be not necessary. The HAP samples were sintered at 1200 °C with a dwell time of 60 min. A pressure of 25 MPa was applied gradually once the sample reached maximum temperature. The SPS was allowed to cool before starting the cleaning process. The part was then placed in a furnace (without vacuum) up to 900 °C and held for 60 min to allow the remaining graphite to decompose (Fig. 3a). Any undesireable surface texture or residual powder was removed from the samples using a media blaster. Glass beads (80–100 grit, Interactivia) were used to finish the ceramic sample and to accentuate the surface features for bone implant applications.

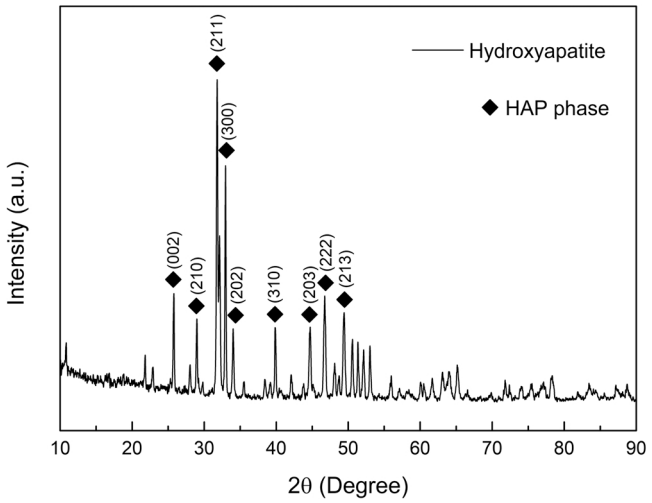

Fig. 5. XRD showing pure HAP phase in final part.

Stainless Steel 316 L (SS316L) was chosen to show the applicability of this method to metallic materials due to its versatility and ubiquitous use in industry. In this case, the graphite sacrificial part was designed in order to create an internal channel in the sintered specimen. A loop made of graphite was produced following the printing procedure described above. It was then inserted into a SPS die and the remaining space was filled with stainless steel powder. The powder assembly was then sintered at 950 °C for 20 min. A pressure of 50 MPa was applied once the sintering temperature was reached (Fig. 3b). Once the component was extracted from the die, the graphite powder was removed in order to reveal the channel inside the specimen.

Density measurements of all components in the sintering cycle (alumina powder, graphite mold, HAP powder, stainless steel powder) were necessary as input parameters for the finite element model. The theoretical densities of the printed powder and mold were determined using a helium gas pycnometer (Ultrapyc 5000, Anton Paar, Austria). Relative densities of printed molds and tap densities of the powders were then determined via the geometrical measurement method. The bulk densities of the sintered parts were estimated using the Archimedes' immersion method following ASTM standard C373–18.

Scanning Electron Microscopy (FEI Quanta 450, FEI, Hillsboro, OR, USA) was performed on polished and etched surfaces to analyze the microstructure of the material; grain size and porosity were assessed. The ceramic sample was thermally etched at 950 °C for 30 min and the metallic surface was chemically etched. An additional step was required for the ceramic parts to confirm the phase composition of the HAP sample. X-Ray Diffraction (Bruker D-8 diffractometer, MA, USA) was used utilizing CuKα radiation at room temperature.

3. SPS modeling of the powder assembly

The sintering behavior of the powder assembly is influenced by the contribution of the different powders that compose it. Therefore, the geometry of the components at the end of sintering cannot be predicted using the mass conservation law. The sintering model embedded in the FEM software (COMSOL Multiphysics®, COMSOL Inc., Los Angeles, CA) allows the prediction of the densification and displacement that occurs during sintering resulting in a useful tool for the design of the initial geometry of the components.

The description of the mechanics of the powder compact was defined using the constitutive relationship of the continuum theory of sintering proposed by Olevsky [37].

$$\sigma_{ij} = \frac{\sigma(W)}{W}\left[\varphi\dot{\varepsilon}_{ij} + \left(\psi - \frac{1}{3}\varphi\right)\dot{e}\delta_{ij}\right] + P_L\delta_{ij} \tag{1}$$

The stress tensor components are σ_{ij} (Pa) and $\sigma(W)$ (Pa) is the effective equivalent stress that determines the constitutive behavior of a porous material. W (s^{-1}) is the equivalent strain rate, $\dot{\varepsilon}_{ij}$ (s^{-1}) represents the strain rate tensor components, φ and ψ are, respectively, the normalized shear and bulk viscosities, P_L (Pa) is the sintering stress, and δ_{ij} is the Kroenecker delta.

The equivalent stress for the SPS of a powder material is based on the power-law creep equation:

$$\sigma(W) = AW^m \tag{2}$$

where m is the strain rate sensitivity exponent, and A (Pa s^m) is the power-law creep coefficient.

$$A = \frac{1}{A_0^m}T^m exp\left(\frac{mQ}{RT}\right) \tag{3}$$

A_0 (K $Pa^{-1/m}$ s^{-1}) is the power creep factor, T (K) is the absolute temperature, R (J mol^{-1} K^{-1}) is the gas constant, and Q (J mol^{-1}) is the power law creep activation energy.

Since the considered process conditions are not sufficient to sinter the graphite powder that composes the sacrificial part, the graphite equivalent stress is based on the conditions of cold compaction where σ_y (Pa) is the yield strength:

$$\sigma(W) = \sigma_y \tag{4}$$

Considering a porous material, the equivalent strain rate, normalized shear, bulk viscosity, and sintering stress are defined as functions of porosity θ:

$$W = \sqrt{\frac{\varphi\dot{\gamma}^2 + \psi\dot{e}^2}{1-\theta}} \tag{5}$$

$$\varphi = (1-\theta)^2 \tag{6}$$

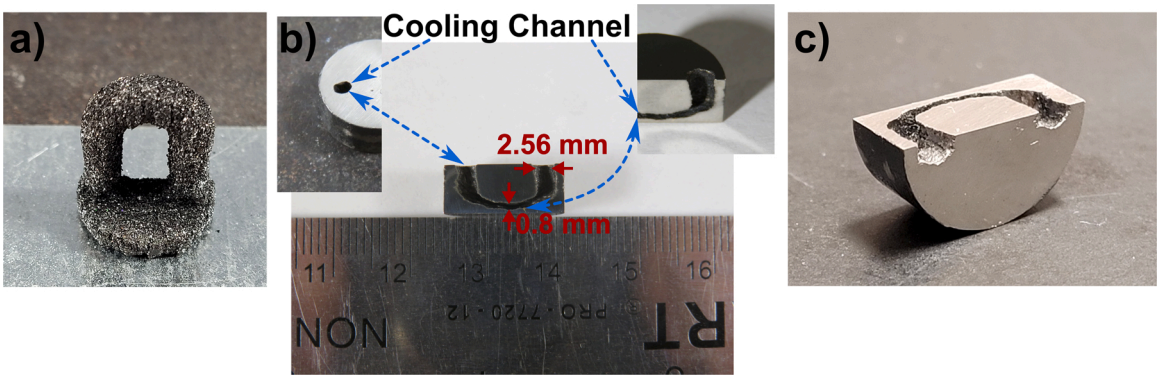

Fig. 6. Stainless-Steel 316 L specimen a) graphite loop b) top and bottom internal channel measurements after SPS c) full cross-section view.

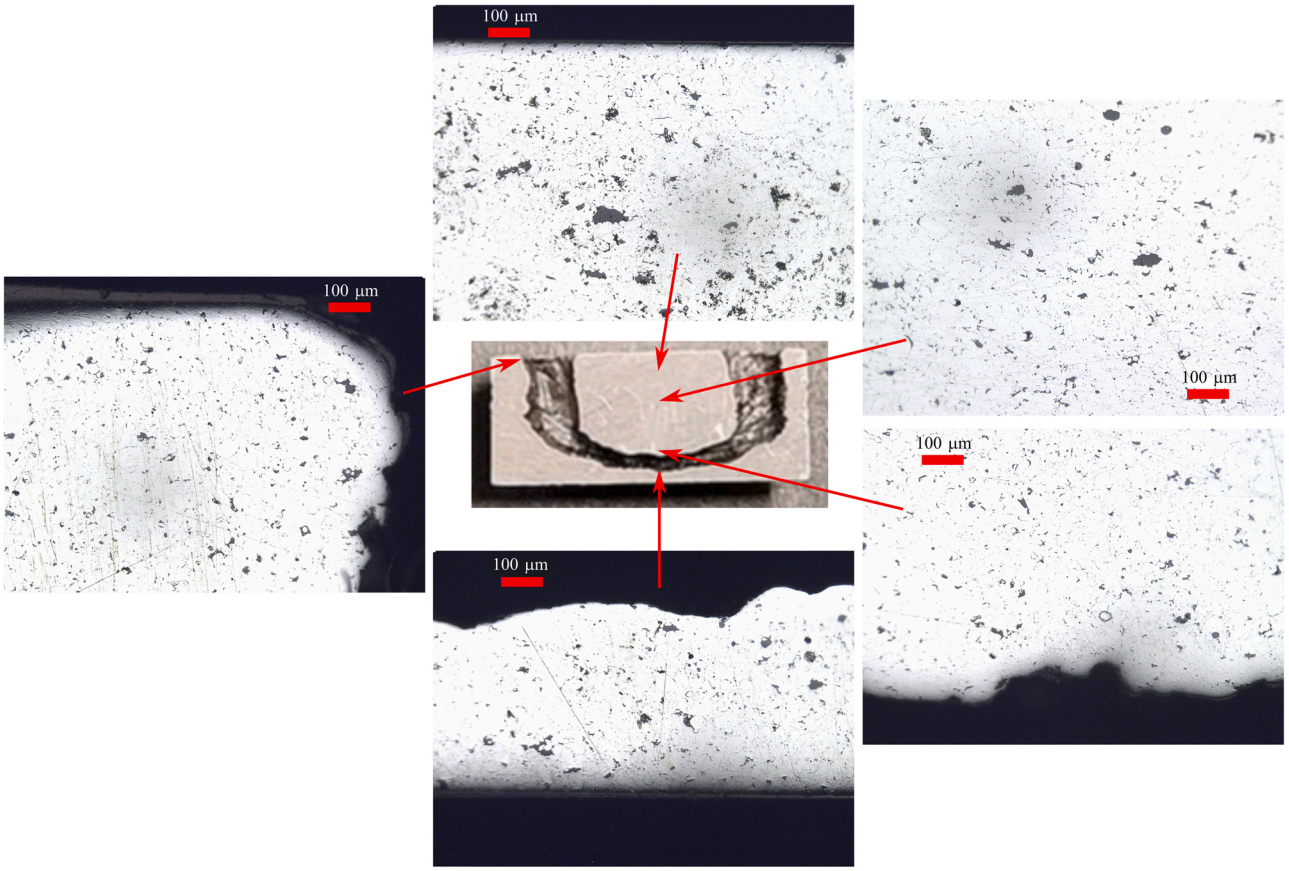

Fig. 7. Micrographs of the Stainless-steel 316 L components in the different areas.

$$\psi = \frac{2}{3}\frac{(1-\theta)^3}{\theta} \tag{7}$$

$$P_L = \frac{3\alpha}{r_0}(1-\theta)^2 \tag{8}$$

where α is the surface energy (J m^{-2}), r_0 is the particles radius (μm) and $\dot{\gamma}$ is the shape change rate.

(s^{-1}) defined as:

$$\dot{\gamma} = \sqrt{2\left(\dot{\varepsilon}_{xy}^2 + \dot{\varepsilon}_{xz}^2 + \dot{\varepsilon}_{yz}^2\right) + \frac{2}{3}\left(\dot{\varepsilon}_x^2 + \dot{\varepsilon}_y^2 + \dot{\varepsilon}_z^2\right) - \frac{2}{3}\left(\dot{\varepsilon}_x\dot{\varepsilon}_y + \dot{\varepsilon}_x\dot{\varepsilon}_z + \dot{\varepsilon}_y\dot{\varepsilon}_z\right)} \tag{9}$$

To determine the sintering parameters (strain rate sensitivity and power law creep coefficient), the sintering materials (HAP, alumina, stainless steel) were sintered separately. Using the method described in work done by Manière at al. [65] that linearize the constitutive equation for the SPS:

$$\frac{1}{m} ln\left(\frac{|\sigma_z|}{\left(\psi + \frac{2}{3}\varphi\right)^{1+\frac{m-1}{2}}(1-\theta)^{\frac{1-m}{2}}}\right) - ln(T) = -ln(A_0) + \frac{Q}{RT} \tag{10}$$

one can identify the A_0 and Q parameters through the regression of the experimental data for a fixed m value.

The graphite mold was considered to be subjected to cold compaction, and in this case the effective equivalent stress is described as:

$$\sigma(W) = \sigma_y \tag{11}$$

Where σ_y [MPa] is the yield strength and the creep parameter $m \sim 0$.

To determine the value of σ_y, the graphite powder was subjected to multi-step pressure dilatometry [66,67].

4. Results

The discussion on the experimental outcomes is provided first as a demonstration of the applicability of the proposed method for both metallic and ceramic materials. The accuracy of the electro-thermal-mechanical simulation used to predict the material behavior of the materials during sintering is discussed later.

A high-density 10 mm diameter ceramic cylinder with 4 channels was successfully produced using a 3D printed graphite mold and Spark Plasma Sintering (Fig. 2). The graphite removal process described above was easy and sufficient in removing the residual graphite. As predicted, the alumina powder and graphite mold did not sinter, leading to easy detachment. The relative density achieved was 96% and the final average grain size was < 1 μm as seen in Fig. 4. The microstructure in the middle and edge of the sample is shown in Fig. 4 for both the 4-channel geometry and the solid (no channel) configuration. The slight difference in grain sizes in the sample with no channels is attributed to the thermal gradient found within the SPS set up; however, the increase in grain size was small because of the fast SPS densification process. The presence of graphite in the internal channels of the sacrificial mold allowed the manipulation of the thermal mass inside the sample; therefore, the heterogeneity of the microstructure seen in the solid sample is not seen in the 4-channel sample. The final HAP samples were analyzed via X-Ray Diffraction (XRD) to confirm HAP was the only phase present as seen in Fig. 5. This result is important in confirming the biocompatibility of HAP for biomedical applications. No carbon diffusion from the graphite mold was present in the HAP part due to the partial debinding step taken prior to sintering.

A fully dense stainless steel cylinder (15 mm diameter and 10 mm height) with an internal curved channel was also manufactured

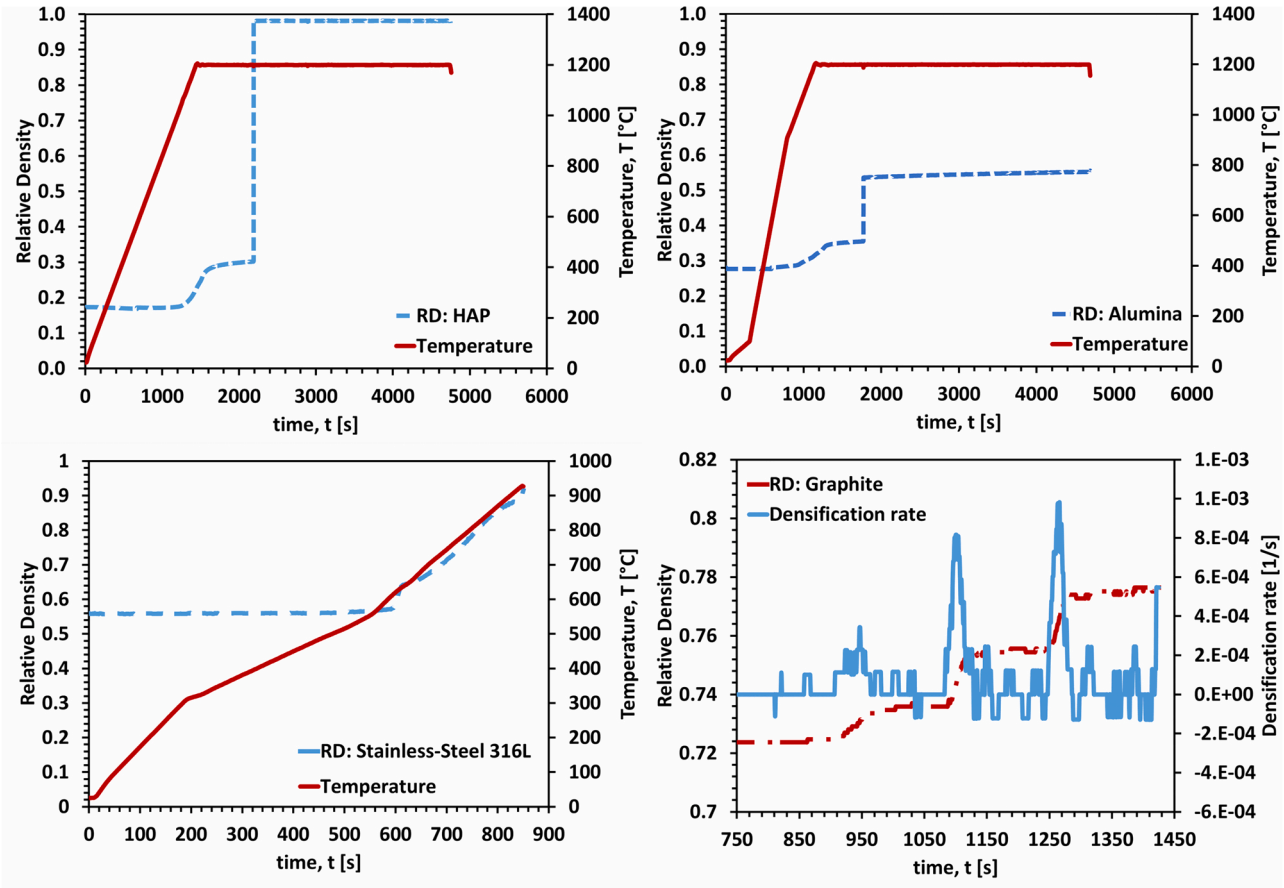

Fig. 8. Densification curve for HAP, alumina and stainless-steel 316 L powders and densification rate for graphite powder.

Table 1
sintering and cold compaction parameters.

Material	A [Pa s]	Q [kJ/K mol]	m	σ_y [MPa]
Alumina	0.0011	172	1	–
HCP	$5.45 \bullet 10^{-4}$	114	1	–
Stainless-Steel 316 L	$1.06 \bullet 10^{-4}$	65.3	1	–
Graphite	–	–	~0	60

successfully using the proposed method. The design of the channel was chosen to represent a possible loop in a component that requires a cooling system; therefore, a curved cylindrical element with a support to easily insert and keep it centered in the die was printed (Fig. 6a). Once the printed element was inserted into the die, it was surrounded by stainless steel powder and then the cylindrical specimen with the presence of the curved graphite element was sintered. The stainless steel (SS) part and the cross-section is shown in The surface roughness of the internal channel is due to the resolution of the printed graphite part. In future work, this will be improved by optimizing the graphite powder and printing. A post-processing step for the polishing of the stainless-steel inner channel may be required depending on the application.

*Figure*6 after cleaning. The surface roughness of the internal channel is due to the resolution of the printed graphite part. In future work, this will be improved by optimizing the graphite powder and printing. A post-processing step for the polishing of the stainless-steel inner channel may be required depending on the application.

Fig. 7 presents the microstructure of the component after polishing in different areas of the sample. These images show how the density is homogeneous in the different areas of the component.

Although the outer geometries shown for both the HAP and stainless-steel samples are discs, changing the outer geometry is possible via the printed graphite mold. As can be seen in Fig. 2, the graphite mold was designed to have straight walls, however, these walls can be designed to be of any geometry. The geometry of the sacrificial mold dictates not only the internal architecture but the external architecture of the samples as well as how to attain a variety of final geometries.

4.1. Model

The densification curves for each material were obtained to determine the densification reached during cold compaction (graphite) and sintering (alumina, HCP and stainless steel) and are shown in Fig. 8.

Using the procedures described in Section 3, the sintering and cold compaction parameters for the different materials were determined (Table 1).

The model's results for the HAP 4-channel component are presented in Fig. 9. It is possible to observe the different densification levels reached by the three materials that compose the initial assembly (graphite, alumina and HAP). The external ring made from alumina reached a final relative density of around 70%, meanwhile the graphite mold was compacted up to 80–85%; therefore, these sacrificial parts were easily removed from the final component which reached full density.

The comparison of the sintered component and model dimension are reported in Table 2.

The comparison between the dimensions of the different geometrical features measured in the real and in the "virtual" component show good agreement with only small differences that can be derived from experimental uncertainty. Some of this uncertainty can be derived from the dimensional precision of the printed mold which was affected by the resolution of the solvent jetting process.

Similarly, the model was run for the stainless steel component with

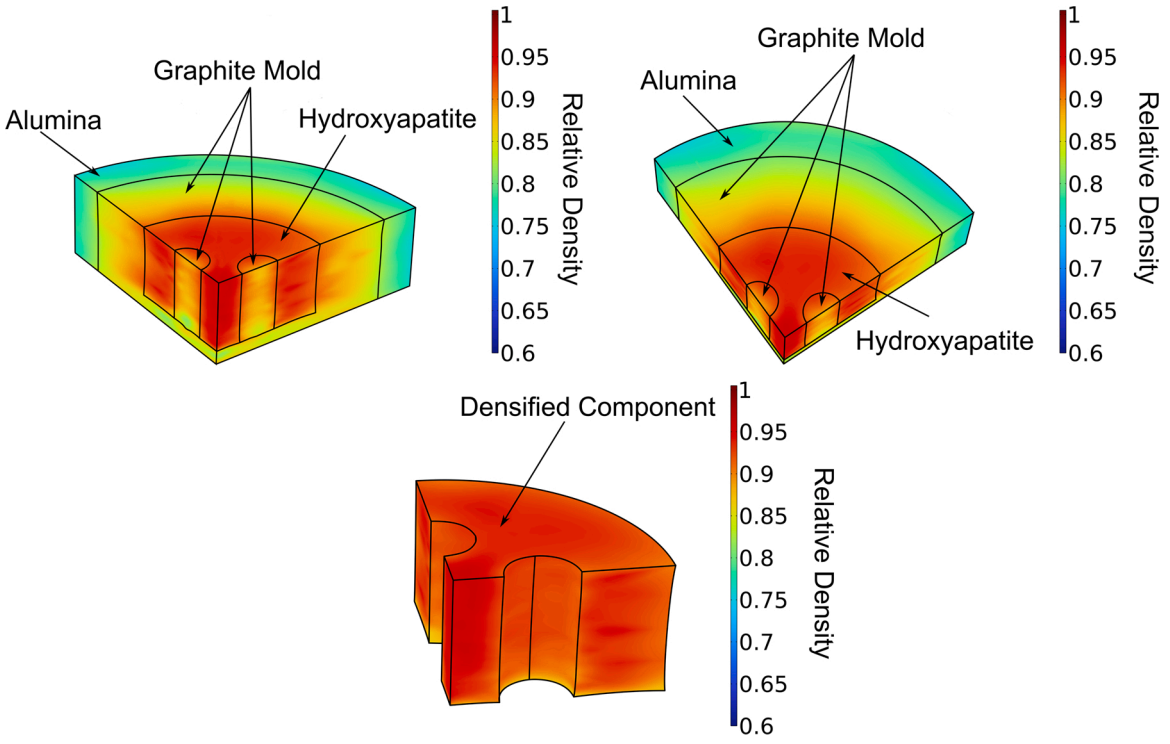

Fig. 9. FEM model results of the 4 channel HCP component.

Table 2
Comparison between experimental and model HCP specimen's dimension.

	Height [mm]	Diameter [mm]	Channel diameter [mm]
Experimental	4.54	15.00	2.30
Model	4.74	14.98	2.63
Δ	0.20	0.02	0.33

the internal loop channel feature. The model results are showed in Fig. 10. Also, for this case, it is possible to appreciate the ability of the model to predict the varying levels of densification of the different materials used in this process.

For the stainless-steel part, the model predicted a final relative density of 98% which was in agreement with the experimental results. Moreover, in Table 3, the comparison between the experimental and the model results for the stainless-steel component are reported.

For both the HAP and the stainless-steel components, the model was capable of predicting the final dimension of the internal channel.

5. Discussion

A novel approach using Spark Plasma Sintering (SPS) and 3D printing via Solvent Jetting (SJ) to manufacture complex shaped metallic and ceramic parts with integrated internal channels has been developed. The proposed approach opens the potential of producing near net shape ceramic and metallic parts in a streamlined process which takes advantage of the ability to design and produce custom complex shapes using the SJ printing method in conjunction with the ability to use SPS to consolidate materials efficiently. The method to SPS a 3D printed graphite mold was validated by producing both a 4-channel HAP ceramic disc and a U-shaped channel stainless steel metallic part. A finite element model was created to simulate the densification behavior of the sample in the graphite mold during sintering. The density and shape of the final sintered samples were accurately predicted by the simulation and can be used in the design of the mold for various materials and components.

This work demonstrates the significant potential that advanced Spark Plasma Sintering methods have in creating complex shapes with a custom internal architecture. Traditionally, SPS was limited by the die geometry where one tooling set was dedicated to the production of one sample shape. Theoretically, any internal and external shape can be printed using the presented method; however, additional experiments need to be conducted to assess the realistic geometric limits. The U-shaped metallic part illustrates the freedom of having features perpendicular to the direction of the load - a common concern in pressure assisted sintering. Furthermore, the 4-channel ceramic part produced in this work addresses the multiple feature ability of this method by having more than one channel. This process can be extended to most materials given that the powder of interest does not need to go through any preparation prior to sintering. Using the developed modeling code, a proper sintering cycle can be determined for each material and geometry, dramatically improving the productivity of the SPS technology.

6. Conclusions

Two components with internal channels and respectively made from hydroxyapatite and stainless steel 316 L powders were manufactured combining the solvent jetting and spark plasma sintering technology. The two components were analyzed to measure the final density and microstructure using SEM. The continuum theory of sintering constitutive equation embedded in COMSOL FEM software was successfully used to predict the sintering behavior of the materials and the final shape of the components and component channels.

Declaration of Competing Interest

The authors declare that they have no known competing financial interests or personal relationships that could have appeared to influence the work reported in this paper.

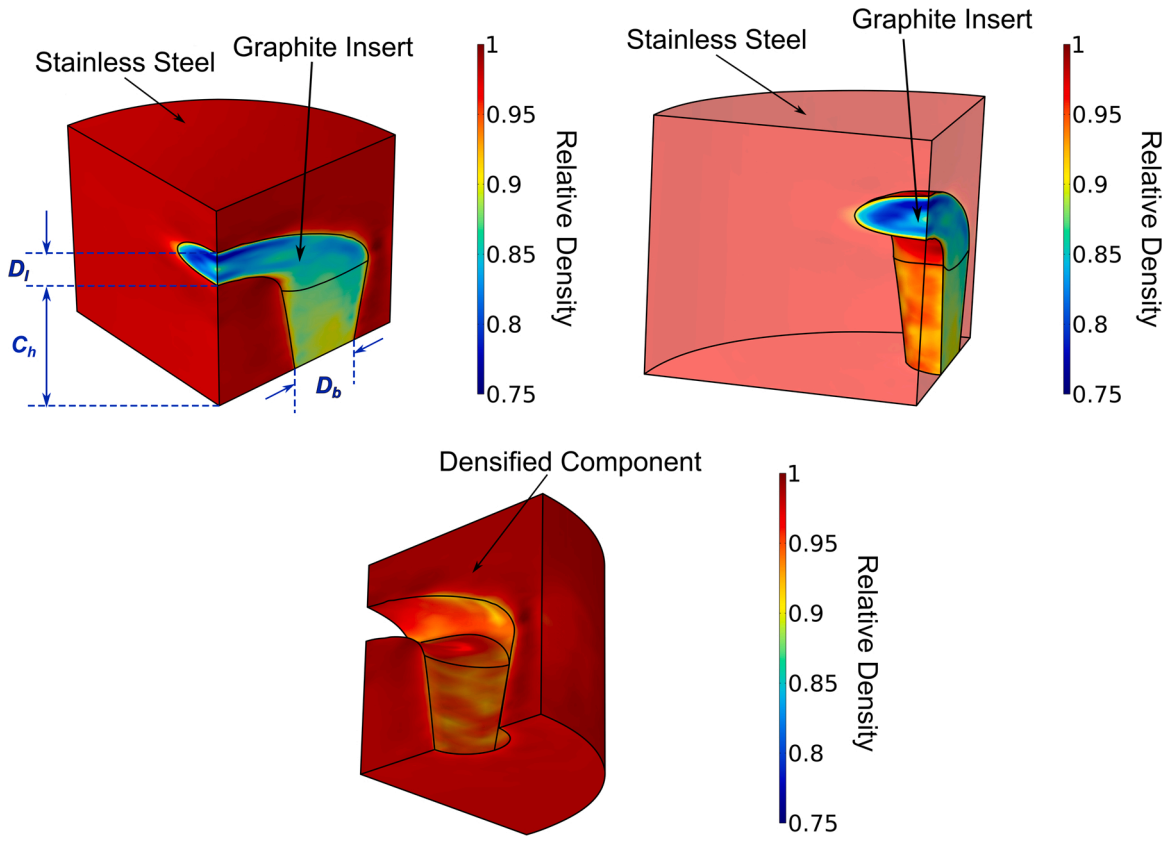

Fig. 10. FEM model results of the Stainless-steel 316 L component.

Table 3
Comparison between experimental and model SS316L specimen's dimensions.

	Bottom Diameter (D_b) [mm]	Loop Diameter (D_l) [mm]	Channel height (C_h) [mm]
Experimental	2.56	0.8	5.18
Model	2.64	1.17	4.45
Δ	0.08	0.37	0.73

Data Availability

The raw/processed data required to reproduce these findings cannot be shared at this time as the data also forms part of an ongoing study.

Acknowledgements

The support of Minority Serving Institutions Science, Technology, Engineering and Mathematics Research and Development Consortium (MSRDC) (Award No: D01-W911-SR-14–2-0023); US Army DEVCOM - Army Research Laboratory (Contract W911-NF-20–2-0226); and the National Science Foundation (Award 2119832) is gratefully acknolwledged.

References

[1] E.A. Olevsky, D.V. Dudina, Field-assisted sintering: science and applications, ISBN 978-3-319-76031-5, Springe Nat. IP (2018) 425.
[2] R. Orrù, R. Licheri, A.M. Locci, A. Cincotti, G. Cao, Consolidation/synthesis of materials by electric current activated/assisted sintering, Mater. Sci. Eng.: R: Rep. 63 (4–6) (2009) 127–287.
[3] Z.A. Munir, U. Anselmi-Tamburini, M. Ohyanagi, The effect of electric field and pressure on the synthesis and consolidation of materials: a review of the spark plasma sintering method, J. Mater. Sci. 41 (3) (2006) 763–777.
[4] M. Nishimura, M. Mitomo, H. Hirotsuru, M. Kawahara, Fabrication of silicon nitride nano-ceramics by spark plasma sintering, J. Mater. Sci. Lett. 14 (1046–1047) (1995) 1046–1047.
[5] S. Grasso, Y. Sakka, G. Maizza, Electric current activated/assisted sintering (ECAS): a review of patents 1906-2008, Sci. Technol. Adv. Mater. 10 (5) (2009), 053001.
[6] O. Guillon, J. Gonzalez-Julian, B. Dargatz, T. Kessel, G. Schierning, J. Räthel, M. Herrmann, Field-assisted sintering technology/spark plasma sintering: mechanisms, materials, and technology developments, Adv. Eng. Mater. 16 (7) (2014) 830–849.
[7] B.-N. Kim, K. Hiraga, K. Morita, H. Yoshida, Effects of heating rate on microstructure and transparency of spark-plasma-sintered alumina, J. Eur. Ceram. Soc. 29 (2) (2009) 323–327.
[8] T. Voisin, J.-P. Monchoux, L. Durand, N. Karnatak, M. Thomas, A. Couret, An innovative way to produce γ-TiAl blades: spark plasma sintering, Adv. Eng. Mater. 17 (10) (2015) 1408–1413.
[9] C. Manière, L. Durand, A. Weibel, G. Chevallier, C. Estournès, A sacrificial material approach for spark plasma sintering of complex shapes, Scr. Mater. 124 (2016) 126–128.
[10] P. Mondalek, L. Silva, M. Bellet, A numerical model for powder densification by SPS technique, Adv. Eng. Mater. 13 (7) (2011) 587–593.
[11] C. Manière, L. Durand, A. Weibel, C. Estournès, Spark-plasma-sintering and finite element method: From the identification of the sintering parameters of a submicronic α -alumina powder to the development of complex shapes, Acta Mater. 102 (2016) 169–175.
[12] H. Kim, O. Gillia, P. Dorémus, D. Bouvard, Near net shape processing of a sintered alumina component: adjustment of pressing parameters through finite element simulation, Int. J. Mech. Sci. 44 (12) (2002) 2523–2539.
[13] C. Manière, E. Nigito, L. Durand, A. Weibel, Y. Beynet, C. Estournès, Spark plasma sintering and complex shapes: The deformed interfaces approach, Powder Technol. 320 (2017) 340–345.
[14] C. Manière, E. Torresani, E.A. Olevsky, Simultaneous spark plasma sintering of multiple complex shapes, Materials 12 (4) (2019) 557.
[15] A. Saini, T. Pollock, High-temperature materials increase efficiency of gas power plants, MRS Bull. 37 (6) (2012) 550–551.
[16] E. Bakan, D.E. Mack, G. Mauer, R. Vaßen, J. Lamon, N.P. Padture, High-Temperature Materials for Power Generation in Gas Turbines. In Advanced Ceramics for Energy Conversion and Storage, Elsevier, 2020, pp. 3–62.
[17] T.M.L. Energetsko, Energy-efficient gas-turbine blade-material technology—a review, Energy 355 (2017) 361.
[18] R.C. Wilcock, J.B. Young, J.H. Horlock, The Effect of Turbine Blade Cooling on the Cycle Efficiency of Gas Turbine Power Cycles, in: J. Eng. Gas Turbines Power, 127, ASME, 2005, pp. 109–120, https://doi.org/10.1115/1.1805549.

[19] B. Sunden, G. Xie, Gas turbine blade tip heat transfer and cooling: a literature survey, Heat. Transf. Eng. 31 (7) (2010) 527–554.
[20] F.N. Nourin, R.S. Amano, Review of gas turbine internal cooling improvement technology, J. Energy Resour. Technol. 143 (8) (2021), 080801.
[21] W. Sixel, M. Liu, G. Nellis, B. Sarlioglu, Ceramic 3D printed direct winding heat exchangers for improving electric machine thermal management, 2019 IEEE Energy Convers. Congr. Expo. (ECCE) (2019) 769–776, https://doi.org/10.1109/ECCE.2019.8913234, doi: https://doi.org/10.1016/j.applthermaleng.2021.116754.
[22] S. Luo, D. Xu, J. Song, J. Liu, A review of regenerative cooling technologies for scramjets, Appl. Therm. Eng. 190 (2021), p116754.
[23] Z. Zou, Y. Wang, P. Du, L. Yao, S. Yang, W. Zhang, J. Luo, A novel simplified precooled airbreathing engine cycle: thermodynamic performance and control law, Energy Convers. Manag. 258 (2022), 115472, https://doi.org/10.1016/j.enconman.2022.115472.
[24] Z.G. Wang, Y. Wang, J.Q. Zhang, B.C. Zhang, Overview of the key technologies of combined cycle engine precooling systems and the advanced applications of micro-channel heat transfer, Aerosp. Sci. Technol. 39 (2014) 31–39, https://doi.org/10.1016/j.ast.2014.08.008.
[25] D. Singh, W. Yu, D.M. France, T.P. Allred, I.H. Liu, W. Du, B. Barua, M.C. Messner, One piece ceramic heat exchanger for concentrating solar power electric plants, Renew. Energy vol. 160 (2020) 1308–1315, https://doi.org/10.1016/j.renene.2020.07.070.
[26] H. Cao, N. Kuboyama, A biodegradable porous composite scaffold of PGA/β-TCP for bone tissue engineering, Bone vol. 46 (2) (2010) 386–395, https://doi.org/10.1016/j.bone.2009.09.031.
[27] N. Sultana, M. Wang, PHBV/PLLA-based composite scaffolds fabricated using an emulsion freezing/freeze-drying technique for bone tissue engineering: surface modification and in vitro biological evaluation, Biofabrication vol. 4 (1) (2012) 15003, https://doi.org/10.1088/1758-5082/4/1/015003.
[28] H. Yoshikawa, N. Tamai, T. Murase, A. Myoui, Interconnected porous hydroxyapatite ceramics for bone tissue engineering, J. R. Soc. Interface vol. 6 (Suppl 3) (. 2009) S341–S348, https://doi.org/10.1098/rsif.2008.0425.focus.
[29] G. Lee, M. Carrillo, J. McKittrick, D.G. Martin, E.A. Olevsky, Fabrication of ceramic bone scaffolds by solvent jetting 3D printing and sintering: Towards load-bearing applications, Addit. Manuf. vol. 33 (2020), 101107, https://doi.org/10.1016/j.addma.2020.101107.
[30] C. Feng, B. Ma, M. Xu, D. Zhai, Y. Liu, J. Xue, J. Chang, C. Wu, Three-dimensional printing of scaffolds with synergistic effects of micro–nano surfaces and hollow channels for bone regeneration, ACS Biomater. Sci. Eng. vol. 7 (3) (. 2021) 872–880, https://doi.org/10.1021/acsbiomaterials.9b01824.
[31] M.H. Carrillo, G. Lee, C. Maniere, E.A. Olevsky, Additive manufacturing of powder components based on subtractive sintering approach, *Rapid Prototyp. J.* (. 2021), https://doi.org/10.1108/RPJ-01-2021-0006. Vol. Ahead–p, no. Ahead–Print.
[32] Y. Yao, W. Qin, B. Xing, N. Sha, T. Jiao, Z. Zhao, High performance hydroxyapatite ceramics and a triply periodic minimum surface structure fabricated by digital light processing 3D printing, J. Adv. Ceram. vol. 10 (1) (2021) 39–48, https://doi.org/10.1007/s40145-020-0415-4.
[33] T. Do, C. Shin, P. Kwon, J. Yeom, Fully-enclosed ceramic micro-burners using fugitive phase and powder-based processing, Sci. Rep. vol. 6 (1) (2016) 31336, https://doi.org/10.1038/srep31336.
[34] M. Bachman, G.P. Li, Integrated MEMS in package, Circuit World vol. 38 (4) (. 2012) 184–192, https://doi.org/10.1108/03056121211280404.
[35] W. Nawrot, K. Malecha, Additive manufacturing revolution in ceramic microsystems, Microelectron. Int. vol. 37 (2) (. 2020) 79–85, https://doi.org/10.1108/MI-11-2019-0073.
[36] A. Díaz Lantada, A. de Blas Romero, M. Schwentenwein, C. Jellinek, J. Homa, J. P. García-Ruíz, Monolithic 3D labs- and organs-on-chips obtained by lithography-based ceramic manufacture, Int. J. Adv. Manuf. Technol. vol. 93 (9) (2017) 3371–3381, https://doi.org/10.1007/s00170-017-0443-6.
[37] E.A. Olevsky, Theory of sintering: from discrete to continuum, Mater. Sci. Eng.: R: Rep. 23 no. 2 (1998) 41–100.
[38] R.K. Bordia, S.-J.L. Kang, E.A. Olevsky, Current understanding and future research directions at the onset of the next century of sintering science and technology, J. Am. Ceram. Soc. 100 (6) (2017) 2314–2352.
[39] M. Abouaf, Finite element simulation of hot isostatic pressing of metal powders, Int. J. Numer. Methods Eng. 25 (1988) 191–212.
[40] E.A. Olevsky, C. Garcia-Cardona, W.L. Bradbury, C.D. Haines, D.G. Martin, D. Kapoor, S.J. Kang, Fundamental aspects of spark plasma sintering: ii. finite element analysis of scalability, J. Am. Ceram. Soc. 95 (8) (2012) 2414–2422.
[41] D. Giuntini, E.A. Olevsky, C. Garcia-Cardona, A.L. Maximenko, M.S. Yurlova, C. D. Haines, D.G. Martin, D. Kapoor, Localized overheating phenomena and optimization of spark-plasma sintering tooling design, Materials 6 (7) (2013) 2612–2632.
[42] D. Giuntini, J. Raethel, M. Herrmann, A. Michaelis, C.D. Haines, E.A. Olevsky, Spark plasma sintering novel tooling design: temperature uniformization during consolidation of silicon nitride powder, J. Ceram. Soc. Jpn 124 (2016) 403–414.
[43] K. Matsugi, H. Kuramoto, T. Hatayama, O. Yanagisawa, Temperature distribution at steady state under constant current discharge in spark sintering process of Ti and Al2O3 powders, J. Mater. Process Technol. 134 (225–232) (2013).
[44] A. Zavaliangos, J. Zhang, M. Krammer, J.R. Groza, Temperature evolution during field activated sintering, Mater. Sci. Eng.: A 379 (1–2) (2004) 218–228.
[45] K. Vanmeensel, A. Laptev, J. Hennicke, J. Vleugels, O. Vanderbiest, Modelling of the temperature distribution during field assisted sintering, Acta Mater. 53 (16) (2005) 4379–4388.
[46] U. Anselmi-Tamburini, S. Gennari, J.E. Garay, Z.A. Munir, Fundamental investigations on the spark plasma sintering/synthesis process, Mater. Sci. Eng.: A 394 (1–2) (2005) 139–148.
[47] G. Molénat, L. Durand, J. Galy, A. Couret, Temperature control in spark plasma sintering: an FEM approach, J. Metall. 2010 (2010) 1–9.
[48] A. Pavia, L. Durand, F. Ajustron, V. Bley, G. Chevallier, A. Peigney, C. Estournès, Electro-thermal measurements and finite element method simulations of a spark plasma sintering device, J. Mater. Process. Technol. 213 (8) (2013) 1327–1336.
[49] J.B. Allen, C. Walter, Numerical simulation of the temperature and stress field evolution applied to the field assisted sintering technique, ISRN Mater. Sci. 2012 (2012) 1–9.
[50] C. Maniere, A. Pavia, L. Durand, G. Chevallier, V. Bley, K. Afanga, A. Peigney, C. Estournès, Pulse analysis and electric contact measurements in spark plasma sintering, Electr. Power Syst. Res. 127 (2015) 307–313.
[51] C. Arnaud, C. Manière, G. Chevallier, C. Estournès, R. Mainguy, F. Lecouturier, D. Mesguich, A. Weibel, L. Durand, C. Laurent, Dog-bone copper specimens prepared by one-step spark plasma sintering, J. Mater. Sci. 50 (22) (2015) 7364–7373.
[52] C. Manière, A. Pavia, L. Durand, G. Chevallier, K. Afanga, C. Estournès, Finite-element modeling of the electro-thermal contacts in the spark plasma sintering process, J. Eur. Ceram. Soc. 36 (3) (2016) 741–748.
[53] X. Wang, S.R. Casolco, G. Xu, J.E. Garay, Finite element modeling of electric current-activated sintering: the effect of coupled electrical potential, temperature and stress, Acta Mater. 55 (10) (2007) 3611–3622.
[54] C. Wang, L. Cheng, Z. Zhao, FEM analysis of the temperature and stress distribution in spark plasma sintering: modelling and experimental validation, Comput. Mater. Sci. 49 (2) (2010) 351–362.
[55] S. Grasso, Y. Sakka, G. Maizza, Pressure effects on temperature distribution during spark plasma sintering with graphite sample, Mater. Trans. 50 (8) (2009) 2111–2114.
[56] S. Muñoz, U. Anselmi-Tamburini, Temperature and stress fields evolution during spark plasma sintering processes, J. Mater. Sci. 45 (23) (2010) 6528–6539.
[57] X. Wei, D. Giuntini, A.L. Maximenko, C.D. Haines, E.A. Olevsky, S.J. Kang, Experimental investigation of electric contact resistance in spark plasma sintering tooling setup, J. Am. Ceram. Soc. 98 (11) (2015) 3553–3560.
[58] E.A. Olevsky, C. Garcia-Cardona, W.L. Bradbury, C.D. Haines, D.G. Martin, D. Kapoor, S.J. Kang, Fundamental Aspects of Spark Plasma Sintering: II. Finite Element Analysis of Scalability, J. Am. Ceram. Soc. 95 (8) (2012) 2414–2422.
[59] G. Maizza, S. Grasso, Y. Sakka, Moving finite-element mesh model for aiding spark plasma sintering in current control mode of pure ultrafine WC powder, J. Mater. Sci. 44 (5) (2009) 1219–1236.
[60] C. Geindreau, D. Bouvard, P. Doremus, Constitutive behaviour of metal powder during hot forming. Part I: Experimental investigation with lead powder as a simulation material, Eur. J. Mech. - A/Solids 18 (4) (1999) 581–596.
[61] D. Giuntini, J. Raethel, M. Herrmann, A. Michaelis, E.A. Olevsky, D. Bouvard, Advancement of Tooling for Spark Plasma Sintering, J. Am. Ceram. Soc. 98 (11) (2015) 3529–3537.
[62] M. Suarez, A. Fernandez, J.L. Menendez, R. Torrecillas, H. U, J. Hennicke, R. Kirchner, T. Kessel, Chall. Oppor. Spark Plasma Sinter.: A Key Technol. A N. Gener. Mater. (2013).
[63] H. Kim, O. Gillia, P. Dorémus, D. Bouvard, Near net shape processing of a sintered alumina component: adjustment of pressing parameters through finite element simulation, Int. J. Mech. Sci. 44 (12) (2002) 2523–2539.
[64] T. Voisin, J.-P. Monchoux, L. Durand, N. Karnatak, M. Thomas, A. Couret, An innovative way to produce γ-TiAl blades: spark plasma sintering, Adv. Eng. Mater. 17 (10) (2015) 1408–1413.
[65] C. Manière, G. Lee, J. McKittrick, S. Chan, E.A. Olevsky, Modeling zirconia sintering trajectory for obtaining translucent submicronic ceramics for dental implant applications, Acta Mater. 188 (2020) 101–107.
[66] W. Li, E.A. Olevsky, J. McKittrick, A.L. Maximenko, R.M. German, Densification mechanisms of spark plasma sintering: multi-step pressure dilatometry, J. Mater. Sci. 47 (20) (2012) 7036–7046.
[67] G. Lee, M.S. Yurlova, D. Giuntini, E.G. Grigoryev, O.L. Khasanov, J. McKittrick, E. A. Olevsky, Densification of zirconium nitride by spark plasma sintering and high voltage electric discharge consolidation: a comparative analysis, Ceram. Int. 41 (10) (2015) 14973–14987.